

JGR Space Physics

RESEARCH ARTICLE

10.1029/2019JA026715

This article is a companion to Ross et al. (2019), <https://doi.org/10.1029/2019JA026716>.

Key Points:

- We construct new models of the wave power from VLF transmitters in the inner magnetosphere using wave data from Van Allen probe A
- The total average wave power from all VLF transmitters lies in the range $3\text{--}9\text{ pT}^2$ in the region $1.3 < L^* < 3.0$
- Approximately 50% of the total wave power from VLF transmitters in the region $1.3 < L^* < 3.0$ comes from the transmitters NWC, NAA, and DHO38

Correspondence to:

N. P. Meredith,
nmer@bas.ac.uk

Citation:

Meredith, N. P., Horne, R. B., Clilverd, M. A., & Ross, J. P. J. (2019). An investigation of VLF transmitter wave power in the inner radiation belt and slot region. *Journal of Geophysical Research: Space Physics*, 124. <https://doi.org/10.1029/2019JA026715>

Received 11 MAR 2019

Accepted 26 APR 2019

Accepted article online 22 JUN 2019

An Investigation of VLF Transmitter Wave Power in the Inner Radiation Belt and Slot Region

Nigel P. Meredith¹ , Richard B. Horne¹ , Mark A. Clilverd¹ , and Johnathan P. J. Ross¹ 

¹British Antarctic Survey, Natural Environment Research Council, Cambridge, UK

Abstract Signals from man-made Very Low Frequency (VLF) transmitters, used for communications with submarines, can leak into space and contribute to the dynamics of energetic electrons in the inner radiation belt and slot region. In this study we use ~ 5 years of plasma wave data from the Van Allen Probe A satellite to construct new models of the observed wave power from VLF transmitters both as a function of L^* and magnetic local time and geographic location. Average power peaks primarily on the nightside of the Earth for the VLF transmitters at low geographic latitudes. At higher latitudes the peak average power extends further in magnetic local time due to more extensive periods of nighttime in the winter months. Nighttime power is typically orders of magnitude more than that observed near noon, implying that loss rates from a given VLF transmitter will also maximize in this region. The observed power from any given VLF transmitter is tightly confined in longitude, with the nightside peak power typically falling by a factor of 10 within 10° longitude of the location of the peak signal. We show that the total average wave power from all VLF transmitters lies in the range $3\text{--}9\text{ pT}^2$ in the region $1.3 < L^* < 3.0$, with approximately 50% of this power emanating from three VLF transmitters, NWC, NAA, and DHO38.

1. Introduction

Energetic electrons in the Earth's radiation belts are confined to two distinct regions or belts. The inner radiation belt, which typically occurs in the region $1.3 < L < 2.0$, is relatively stable. In sharp contrast, the outer radiation belt, which typically occurs in the region $2.0 < L < 7.0$, is highly dynamic with fluxes varying by several orders of magnitude on timescales ranging from minutes to weeks (e.g., Baker et al., 1994; Blake et al., 1992). The two belts are separated by a slot region that is usually devoid of electrons.

During strong geomagnetic storms, such as the Halloween storms in 2003, the slot region may become filled and the inner belt flux may increase significantly. For example, during the Halloween storms the flux of relativistic 2- to 6-MeV electrons in the slot region increased by 5 orders of magnitude (Baker et al., 2007). Remarkably, the inner belt flux also increased significantly during the Halloween storms, with a factor of fifty increase at $L = 1.5$, producing a “new” inner zone. Following these enhancements, the fluxes subsequently decay on timescales ranging from days to years, depending on location and energy (Baker et al., 2007).

Understanding the behavior of energetic electrons in the inner radiation belt and slot region is becoming increasingly important from a practical point of view, as the satellite industry evolves and either exploits or sends new satellites through this region. For example, Société Européenne des Satellites now operate 20 satellites at $L = 2.2$, as part of their O3b network in Medium Earth Orbit, designed to deliver satellite internet services to emerging markets. Furthermore, new developments in electric orbit raising (Horne & Pitchford, 2015) mean that satellites designed for geosynchronous orbit now spend a significant portion of time in this potentially damaging regime on their way to their destination orbit.

To help model the behavior of energetic electrons ($E \geq 100\text{ keV}$) in the inner radiation belt and slot region, knowledge is required of relevant source and loss processes. Sources include nondiffusive radial transport by increased large-scale magnetospheric electric fields (Selesnick et al., 2016; Su et al., 2016) and local wave-particle acceleration (Albert et al., 2016). Loss processes include Coulomb collisions and wave-particle interactions. Close to the planet, Coulomb collisions with atmospheric constituents dominate, with the radial extent depending on energy, but this mechanism does not account for the observed decay rates at larger L (Walt, 1964). Electron scattering in the bulk of the inner radiation belt and the slot region is due to resonant interactions with whistler mode waves (e.g., Abel & Thorne, 1998a). The whistler mode waves in

this region can be classified as three distinct types, plasmaspheric hiss, lightning-generated whistlers, and anthropogenic Very Low Frequency (VLF) transmitters.

Plasmaspheric hiss is a broadband, electromagnetic emission that is observed in the plasmasphere and plasmaspheric plumes in the frequency range from 10 Hz to several kilohertz (Li et al., 2015). Broadband amplitudes of plasmaspheric hiss typically range from 100 pT² or less during quiet conditions to > 10⁴ pT² during active periods (Meredith et al., 2004, 2018; Smith et al., 1974; Thorne et al., 1974, 1977). Plasmaspheric hiss is observed at all local times but tends to maximize on the dayside during geomagnetically active conditions (Li et al., 2015; Malaspina et al., 2016; Meredith et al., 2004, 2018; Tsurutani et al., 2015). In contrast, the signals from lightning-generated whistlers are weaker, do not depend on geomagnetic activity, and are strongest on the nightside with intensities of a few picoteslas squared (Meredith et al., 2006). Narrow-band signals from ground-based VLF transmitters, the majority of which operate in the frequency range 18–27 kHz, can leak into the magnetosphere, where they also propagate in the whistler mode. The strongest wave power tends to be confined to the nightside in the region $1.2 < L^* < 2.7$ (Clilverd et al., 2008; Ma et al., 2017), with average peak power the order of several picoteslas squared (Abel & Thorne, 1998a; Ma et al., 2017).

Plasmaspheric hiss is largely responsible for the formation of the slot region between the inner and the outer radiation belts (Abel & Thorne, 1998a, 1998b; Albert, 1994; Lyons et al., 1972; Lyons & Thorne, 1973; Meredith et al., 2007). Plasmaspheric hiss alone can explain the observed losses of 2- to 6-MeV electrons in the outer slot region, but, further in, a combination of plasmaspheric hiss and guided whistlers is necessary to explain the observations (Meredith et al., 2009). In the inner radiation belt the minimum resonant energies for first-order resonance with plasmaspheric hiss and lightning-generated whistlers typically exceed 500 keV (Abel & Thorne, 1998a) and losses of electrons with energies in the region 100–800 keV are primarily controlled by resonant wave-particle interactions with VLF transmitters and Coulomb collisions which take over at the lowest L shells. Indeed, narrow peaks in the spectrum of energetic electrons in the drift loss cone in the inner radiation belt have long been attributed to pitch angle scattering by VLF transmitters (Datlowe & Imhof, 1990; Datlowe et al., 1995; Gamble et al., 2008; Imhof et al., 1983; Inan et al., 1985; Selesnick et al., 2013; Vampola & Kuck, 1978), highlighting the importance of these waves on long-term electron loss in this region.

Ma et al. (2017) recently developed a model of VLF transmitters, which they combined with previous statistical models of plasmaspheric hiss and lightning-generated whistlers (Li et al., 2015; Spasojevic et al., 2015) to estimate pitch angle diffusion rates and lifetimes in the inner radiation belt and slot region. Specifically, Ma et al. (2017) determined the average wave power from VLF transmitters in the equatorial ($\lambda_m < 20^\circ$) inner magnetosphere, integrated from 15 to 30 kHz, as a function of L , magnetic local time (MLT), local season, and geomagnetic activity. However, the observed power in the equatorial magnetosphere at any given time and any given point (L , MLT) in space will also depend on the location of the individual VLF transmitters at that time; that is, there will be a geographic dependence. Furthermore, to calculate diffusion coefficients, Ma et al. (2017) determined average spectral profiles by fitting Gaussian profiles to the wave intensity as a function of frequency at $L = 1.5, 2.0,$ and 2.5 . Power from individual transmitters is thus combined, both in the determination of the average power and in the determination of the spectral profiles.

In this study we use data from the Van Allen Probe A to determine the average wave power spectral densities both as a function of L^* and MLT and geographic location for each individual VLF transmitter. The purpose is to assess the contribution of each VLF transmitter to the total wave power and to build a model that can be used to assess how the geographic and MLT dependence should be taken into account when modeling the contribution of VLF transmitters to electron loss in the inner radiation belt and slot region (Ross et al., 2019). The instrumentation and data analysis techniques used to develop the model are described in section 2, and the VLF transmitters used in the analysis are introduced in section 3. The global morphology of the VLF transmitters is presented in section 4, both as a function of L^* and MLT and as a function of the geographic latitude and longitude of the magnetic footprints of the satellite. The average wave intensities as a function of L^* for each VLF transmitter are presented in section 5. Finally, the results are discussed and the conclusions presented in sections 6 and 7, respectively.

2. Instrumentation and Data Analysis

The Van Allen Probes were launched on 30 August 2012 into highly elliptical orbits with a perigee of $\sim 1.1 R_E$, an apogee of $\sim 5.8 R_E$, and an inclination of 10° (Mauk et al., 2012). The satellites each have an orbital period of ~ 9 hr and sweep through the inner radiation belt and slot region approximately five times per day, making them ideally suited to studies of the plasma waves in this important region.

For this study we use data from the Electric and Magnetic Field Instrument Suite and Integrated Science (EMFISIS; Kletzing et al., 2013) onboard Van Allen Probe A. The wave electric field of the VLF transmitter signals is measured using the wave high-frequency receiver (HFR). This instrument provides measurements of one component of the wave electric field in the plane perpendicular to the spin axis in 82 logarithmically spaced frequency bins in the frequency range 10 to 487 kHz every 6 s. The HFR wave data from Van Allen Probe A have a slightly higher noise floor and more interference lines than those from Van Allen probe B. However, the noise floor is less than $10^{-16} \text{ V}^2 \cdot \text{m}^{-2} \cdot \text{Hz}^{-1}$, which is 4 or more orders of magnitude less than the peak signals from the VLF transmitters, and there are no interference lines in the frequency range 18.21–28.05 kHz used in this study. For our statistical study we use approximately 5 years of EMFISIS data from 26 October 2012, after the complete deployment of the electric field booms, to 31 August 2017.

For comparison with published wave magnetic field intensities and for use in diffusion calculations, we also convert the wave electric field to the wave magnetic field. This requires knowledge of the electron gyrofrequency (f_{ce}) and the electron plasma frequency (f_{pe}). The former is determined directly from the 1-s fluxgate magnetometer measurements of the local magnetic field. The electron plasma frequency is derived from the HFR data and provided as a Level 4 data product. When visible, it is derived from the upper hybrid frequency and elsewhere from the lower-frequency limit of the continuum radiation (Kurth et al., 2015).

The average wave electric field power spectral density and the corresponding number of samples were binned as a function of frequency, half orbit, and L^* in steps of $0.02L^*$. For the global mapping we binned the MLT, the magnetic latitude (λ_m), the geographic latitude and longitude of the northern and southern field line footprints, and the geomagnetic activity as monitored by the *AE* index at the same resolution. L^* , which is related to the third adiabatic invariant (Roederer, 1970), MLT, and the magnetic footprints were computed using the Olson-Pfizer tilt-dependent static model (Olson & Pfizer, 1977) and the International Geomagnetic Reference Field (IGRF) field. Since L^* is calculated for particles and we are using it for waves, we assumed a local pitch angle of 90° in the determination of L^* . For the wave electric field to wave magnetic field conversion, we also binned f_{ce} , f_{pe} , and the corresponding numbers of samples at the same resolution.

3. VLF Transmitters

Man-made VLF transmitters are used for communications with submarines. They mostly operate in the frequency range from 18 to 27 kHz. VLF transmitter sites typically cover large areas, of the order of many square kilometers, with transmitted power ranging from 20 kW to 2 MW. Submarines receive the signal using a towed antenna that floats just beneath the surface. A portion of the VLF transmitter signals propagate through the ionosphere and into the magnetosphere. Here they may interact with radiation belt electrons, primarily in the inner radiation belt and slot region. The majority of VLF transmitters are located on geomagnetic field lines in the range $1.2 < L^* < 3.0$. VLF transmitter signals are typically modulated with minimum shift keying, in which the frequency takes one of two values, representing a binary signal. Many VLF transmitters operate with a bit duration of 5 ms and a ± 50 -Hz frequency shift but covering ± 100 Hz of spectrum from the nominal center frequency (Cohen et al., 2009).

A list of the VLF transmitter signals studied in this analysis are tabulated in Table 1. For each VLF transmitter the table lists its call sign, location, frequency, geographic coordinates, and power. The table also lists the L value and universal time (UT) when the transmitter is at midnight MLT, calculated 100 km above each transmitter, using the Definitive Geomagnetic Reference Field (DGRF) model. The HFR frequency bins that include signals from the VLF transmitters are tabulated in Table 2. The bandwidths of the frequency bins, which range from 900 Hz to 1.31 kHz, are larger than the bandwidths of the VLF transmitter signals, and a given frequency bin typically contains signals from more than one transmitter. To help interpret the results, the VLF transmitters whose central frequencies lie in each frequency bin are included in Table 2.

Table 1
List of VLF Transmitters

Name	Location	Frequency (kHz)	Geographic coordinates (°)	Power (kW)	L	UT when transmitter is at midnight MLT
HWU	Rosnay, France	18.3	46.714119°N 1.244309°E	200	1.81	23.22
GQD	Anthorn, Cumbria, UK	19.6	54.911683°N 3.278738°W	100	2.66	23.39
NWC	Exmouth, W. Australia	19.8	21.816325°S 114.16546°E	1,000	1.42	16.70
ICV	Isola di Tavolara, Italy	20.3	40.923127°N 9.731011°E	50	1.48	22.73
FTA2	Sainte Assise, France	20.9	48.544632°N 2.579429°E	~50	1.95	23.11
NPM	Lualualei, Hawaii, USA	21.4	21.420382°N 158.153912°W	600	1.17	11.04
GVT	Penrith, UK	22.1	54.731799°N 2.883033°W	100	2.64	23.36
JJI	Ebino, Japan	22.2	32.092247°N 130.829095°E	100	1.25	15.57
DHO38	Rhauderfehn, Germany	23.4	53.087341°N 7.608652°E	300	2.38	22.72
NAA	Cutler, Maine, USA	24.0	44.644506°N 67.284565°W	1,000	2.74	4.27
NLK	Seattle, Washington, USA	24.8	48.203633°N 121.916828°W	250	2.88	8.63
unid25	Mokpo, South Korea	25.0	34.679068°N 126.445383°E	250	1.32	15.84
NML	LaMoure, North Dakota, USA	25.2	46.365987°N 98.335667°W	250	3.19	6.76
TBB	Bafa, Turkey	26.7	37.412725°N 27.323342°E	~100	1.39	21.65

Note. UT = universal time; MLT = magnetic local time.

4. Global Morphology

Previous observations have shown that the wave power from a particular VLF transmitter observed in the equatorial magnetosphere is strongest at night in the vicinity of the VLF transmitter, (e.g., Clilverd et al., 2008). In this section we examine the variation of the observed equatorial wave power both as a function of magnetic coordinates (L^* , MLT) and geographic coordinates to assess the contribution of each VLF transmitter to the wave power observed in the equatorial inner magnetosphere.

4.1. MLT Distribution

To investigate the MLT distribution, we determine the average wave electric field power spectral densities as a function of L^* , MLT, and geomagnetic activity for the HFR frequency bins tabulated in Table 2. We initially inspected plots of the average wave electric field power spectral densities as a function of L^* and MLT for each frequency bin for six geomagnetic activity levels, monitored by the AE index (not shown). We found that the average wave power increased on the dawnside during active conditions ($300 < AE < 1,000$ nT) in each frequency bin. This is illustrated in Figure 1, which shows the average wave electric field power spectral density in the frequency bin 19.11–20.05 kHz as a function of L^* and MLT for $AE < 300$ nT (Figure 1a) and for $300 < AE < 1,000$ nT (Figure 1b). Here the power spectral densities have been averaged over all geographic

Table 2
List of the HFR Frequency Bins Used in this Study

Frequency bin (kHz)	VLF transmitters
18.21–19.11	HWU
19.11–20.05	GQD, NWC
20.05–21.03	ICV, FTA2
21.03–22.07	NPM
22.07–23.15	GVT, JJI
23.15–24.29	DHO38, NAA
24.29–25.58	NLK, unid25, NML
25.58–26.74	TBB
26.74–28.05	

Note. HFR = high-frequency receiver.

longitudes for $|\lambda_m| < 20^\circ$. The maps extend linearly out to $L^* = 4$ with noon at the top and dawn to the right. The average power spectral densities are shown in the large panels and the corresponding sampling distributions in the small panels. Strong wave power is seen during active conditions, $300 < AE < 1,000$ nT, on the dawnside beyond $L^* = 2.5$ (Figure 1b) which is entirely absent during quieter conditions, $AE < 300$ nT (Figure 1a). These enhancements, which are seen in each frequency bin used in this study, are unrelated to the VLF transmitter signals and are due to whistler mode chorus, which becomes enhanced on the dawnside during active conditions (Li et al., 2011; Meredith et al., 2001; 2012). To exclude these emissions from our study, we restrict our analysis to periods when $AE < 300$ nT. There is also some enhanced wave power on the duskside in the region 17–22 MLT around $L^* = 2.7$ –2.9. These emissions are unlikely to be chorus as they are not substorm dependent, and they peak in a region that is not usually associated with chorus emissions (Li et al., 2011; Meredith et al., 2001; 2012). They are most likely related to lightning-generated whistlers, which peak in the premidnight sector and do not exhibit a significant dependence on substorm activity (e.g., Meredith et al., 2006). Since the signature is relatively weak when compared to the signals from the VLF transmitters and is even less apparent at other frequencies (Figure 2), we do not attempt to remove it from the study.

The MLT distribution of the average wave electric field power spectral density in each frequency bin is shown as a function of L^* and MLT for $AE < 300$ nT in Figure 2, in the same format as Figure 1. The power spectral

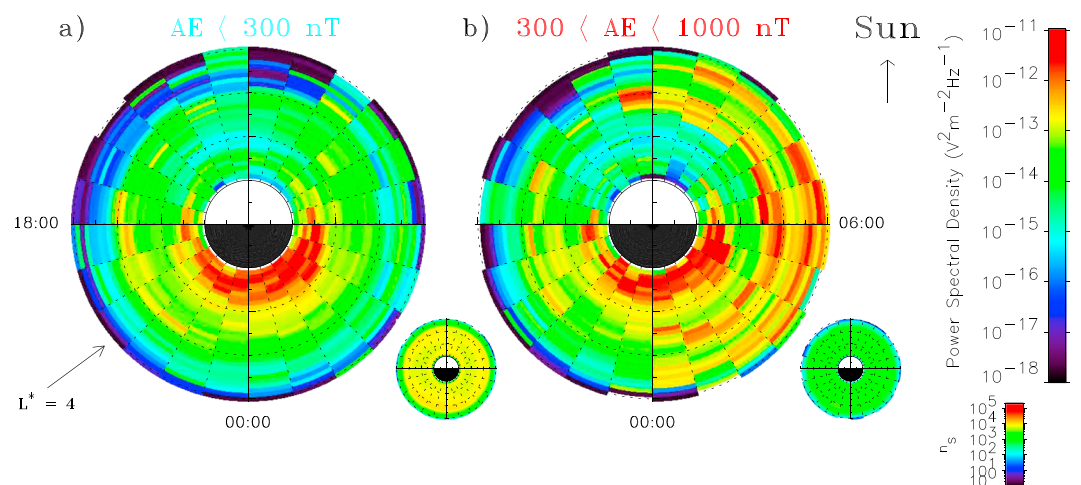


Figure 1. Plots of the average wave electric field power spectral densities as a function of L^* and magnetic local time for the frequency bin 19.11–20.05 kHz for $AE < 300$ nT (a) and $300 < AE < 1,000$ nT (b). Each map extends linearly out to $L^* = 4$ with noon at the top and dawn to the right. The average power spectral densities are shown in the large panels and the corresponding sampling distributions in the small panels.

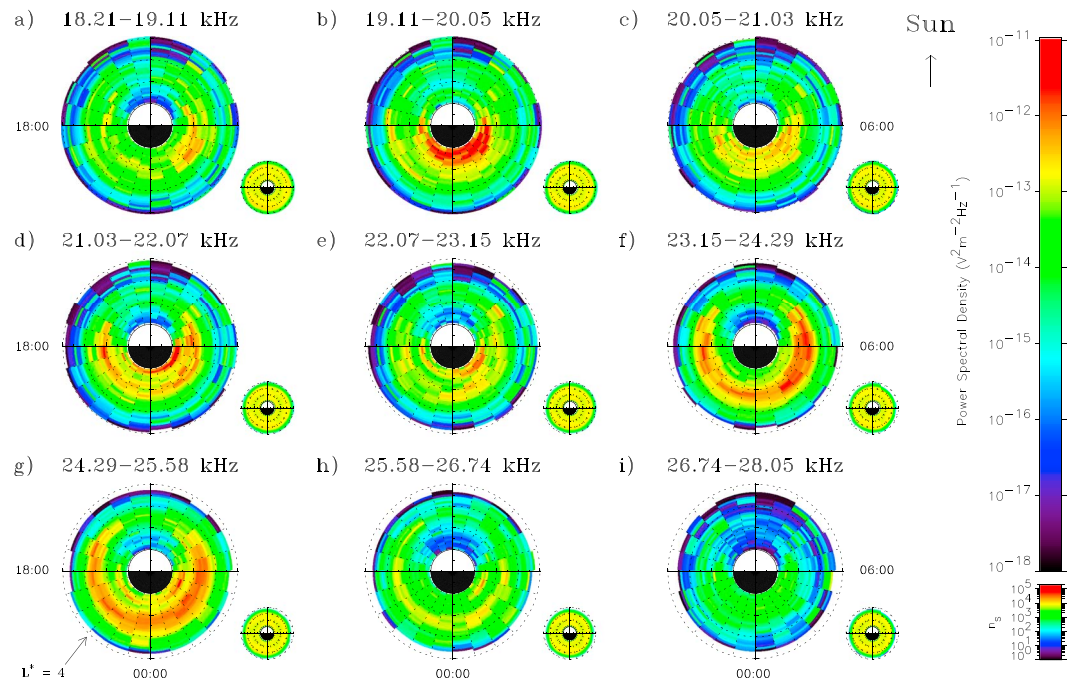


Figure 2. Plots of the average wave electric field power spectral densities as a function of L^* and magnetic local time for each relevant frequency channel, plotted in order of increasing frequency and ranging from 18.21–19.11 kHz (a) to 26.74–28.05 kHz (i). Each map extends linearly out to $L^* = 4$ with noon at the top and dawn to the right. The average power spectral densities are shown in the large panels and the corresponding sampling distributions in the small panels.

densities have again been averaged over all geographic longitudes for $|\lambda_m| < 20^\circ$. Strong wave power at low L^* , $L^* < 1.7$, is seen in Figures 2b, 2d, 2e, and 2g. This strong wave power is associated with VLF transmitters located inside $L^* = 1.5$, namely, NWC, NPM, JJI, and unid25, respectively. The power peaks on the nightside (18–06 MLT), where it tends to be strongest and most extensive in the postmidnight sector (00–06 MLT). Strong wave power at higher L^* , $L^* > 2.0$ is seen primarily in Figures 2f and 2g. This strong wave power is associated with the strongest VLF transmitters located outside $L^* = 2.0$, namely, DHO38, NAA, NLK, and NML. In contrast, the region of strong average wave power from these VLF transmitters is more extensive in local time, typically ranging from 16 MLT through midnight to 08 MLT. In all cases the minimum wave power is observed around noon local time, where it is typically orders of magnitude less than the observed power on the nightside, due to the significant increase in absorption in the sunlit ionosphere (Cohen et al., 2012; Helliwell, 1965).

4.2. Geographic Distribution

To investigate the geographic dependence, we determine the average wave electric field power spectral densities on the nightside (18–06 MLT), where the wave power maximizes, as a function of the geographic latitude and longitude of the satellite footprints in the Northern and Southern Hemispheres. The results are shown, for each frequency bin, in Figure 3. Here the wave power observed in the equatorial magnetosphere has been mapped to the magnetic footprints of the satellite along the magnetic field lines using the Olson-Pfizer tilt-dependent static model (Olson & Pfizer, 1977) and the IGRF field. We assume no loss of power and do not attempt to include the effects of the convergence in the magnetic field. We again use data within the magnetic latitude range $|\lambda_m| < 20^\circ$ and for $AE < 300$ nT. Each tabulated VLF transmitter can be clearly identified, with the wave power maximizing in the vicinity of the VLF transmitter and its conjugate point. Significant wave power from a given VLF transmitter can sometimes be seen in neighboring frequency bins as is the case for NWC, GVT, NAA, NML, and unid25. Superimposed on the enhanced patches of VLF transmitter power is the geographic distribution of lightning-generated whistlers, which tend to maximize over land and minimize over the oceans (e.g., Meredith et al., 2006). This is most clearly seen in Figure 3i.

To investigate the geographic dependence in more detail, we determine the average wave electric field power spectral densities as a function of geographic longitude in the Northern Hemisphere for different L^* bins

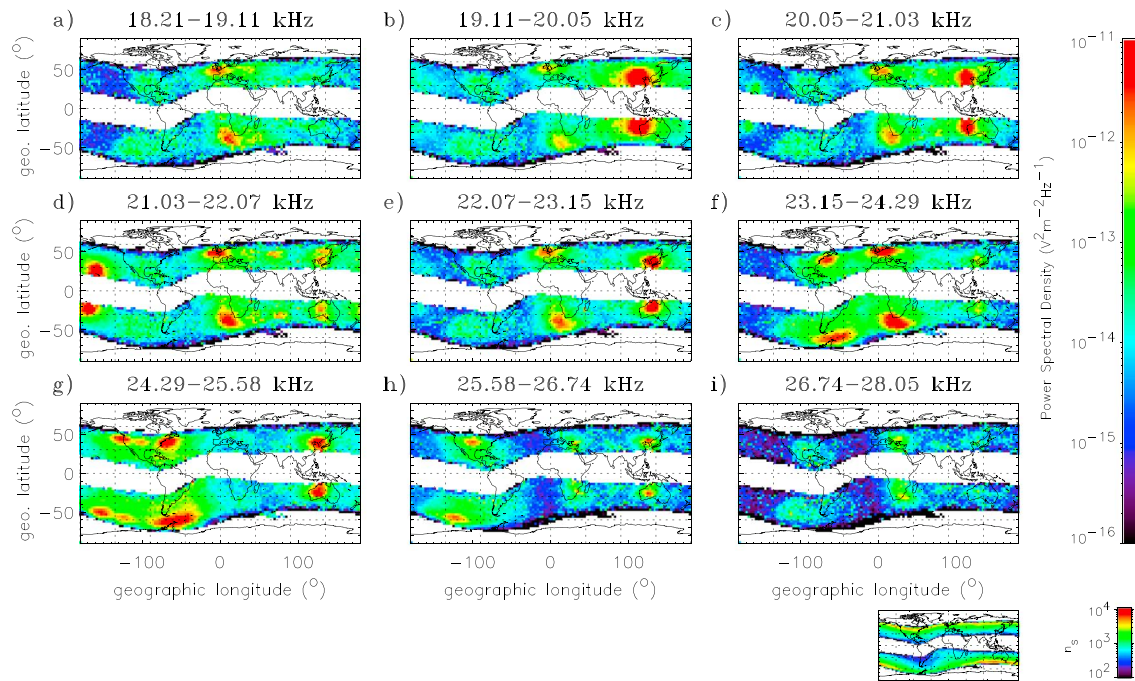


Figure 3. Plots of the average wave electric field power spectral densities on the nightside, where the wave power maximizes, mapped to the conjugate points of the satellite and displayed as a function of geographic latitude and longitude. The plots are presented in order of increasing frequency, ranging from 18.21–19.11 kHz (a) to 26.74–28.05 kHz (i). A representative sampling distribution is shown in the small panel at the bottom of the figure.

ranging from 1.2 to 2.6 in steps of $0.1L^*$. The results are shown in Figure 4. The observed power from any given VLF transmitter is tightly confined in longitude, with the nightside peak power typically falling by a factor of 10 within 10° longitude of the location of the peak signal. The peak power spectral densities cover 2 orders of magnitude, ranging from $10^{-12} \text{ V}^2 \cdot \text{m}^{-2} \cdot \text{Hz}^{-1}$ for TBB (Figure 4h) to $10^{-10} \text{ V}^2 \cdot \text{m}^{-2} \cdot \text{Hz}^{-1}$ for NWC (Figure 4b). The relatively powerful VLF transmitters located at low L^* , $L^* < 1.5$, NWC, NPM, JJI, and unid25 all have peak power spectral densities above $10^{-11} \text{ V}^2 \cdot \text{m}^{-2} \cdot \text{Hz}^{-1}$ (Figures 4b, 4d, 4e, and 4g, respectively). The strongest signals from VLF transmitters located at larger L^* come from DHO38, NAA and NLK, all of which have peak power spectral densities greater than $10^{-11} \text{ V}^2 \cdot \text{m}^{-2} \cdot \text{Hz}^{-1}$ (Figures 4f, 4g, and 4g, respectively). There is also a strong signature that peaks near 5°W in the 21.03- to 22.07-kHz bin (Figure 4d) that is due to signals from a combination of European transmitters, namely, GVT whose central frequency lie close to the bin edge and HWU, which occasionally operates at 21.75 kHz. Significant power from some of the other VLF transmitters is also distributed between neighboring frequency bins, as can be seen for NWC, NAA, NML, and unid25 in Figures 4c, 4g, 4g, and 4h, respectively. Indeed, the signal from NML is sandwiched between NLK and NAA in Figure 4g but appears as an isolated peak in Figure 4h. It is important to take into account this additional power when assessing the power spectral densities of these VLF transmitters.

4.3. Dependence on Geomagnetic Activity

To investigate if the VLF transmitter power observed in the inner magnetosphere has a dependence on geomagnetic activity, we determine the average wave electric field power spectral densities on the nightside as a function of geographic longitude for six representative L^* values and six different geomagnetic activity levels. The results are shown in Figure 5 for the frequency band 22.07–23.15 kHz, where the power spectral densities are plotted as a function of geographic longitude and AE (color coded) for $L^* = 1.4$ to 2.4 in steps of $0.2L^*$. The power spectral densities are shown in the large panels and the corresponding sampling distributions in the small panels. This frequency bin principally contains signatures from JJI and GVT. The strongest signal from JJI is seen around 130°E at $L^* = 1.4$ (Figure 5a) and exhibits little or no dependence on AE . The signal from GVT peaks around 0°E in the region $2.0 < L^* < 2.4$ (Figures 5d to 5f) and also shows little or no dependence on AE . We find a similar lack of dependence on geomagnetic activity for the other VLF transmitters (not shown) and conclude that the observed VLF transmitter power has no significant dependence on substorm activity as monitored by the AE index.

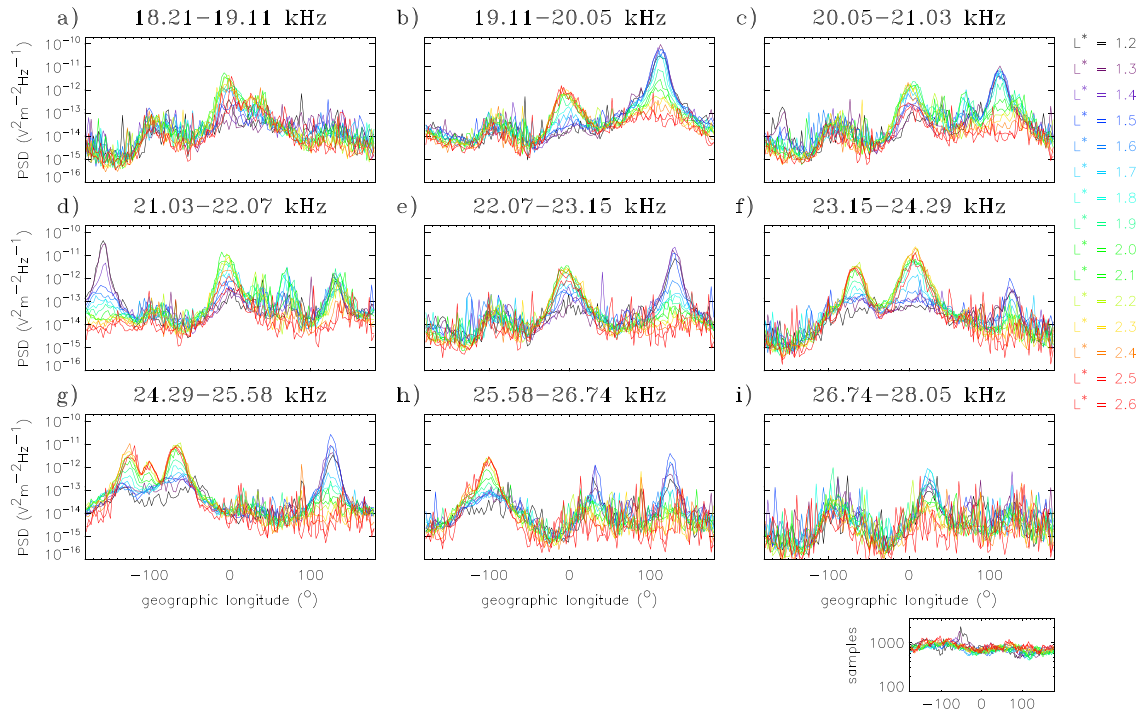


Figure 4. Plots of the average wave electric field power spectral densities on the nightside, where the wave power maximizes, mapped to the northern footprint of the satellite and displayed as a function of geographic longitude for different L^* bins ranging from 1.2 to 2.6 in steps of $0.1L^*$. The plots are presented in order of increasing frequency, ranging from 18.21–19.11 kHz (a) to 26.74–28.05 kHz (i). A representative sampling distribution is shown in the small panel at the bottom of the figure.

5. Average Wave Magnetic Field Intensities

For diffusion model calculations and to compare with previous models that have used the wave magnetic field intensities, we need to convert the electric field wave power spectral densities to the average magnetic field wave power as a function of L^* for each VLF transmitter. To do this, we first calculate the average wave electric field intensity for each VLF transmitter as a function of L^* and then convert to the average wave magnetic field intensity assuming parallel propagation. We convert average electric field intensities rather than the individual measurements since f_{pe} , required for the conversion, is not always available. When averaging the power spectral densities over MLT and geographic longitude for any given VLF transmitter, it is important to exclude wave power from additional VLF transmitters radiating at a nearby frequency. Since the bulk of the wave power from a given VLF transmitter is restricted to a longitude range of $\pm 15^\circ$ centered on the VLF transmitter footprint (Figure 4), we include this power in our longitude averaging and assume that the power from the VLF transmitter is zero at other longitudes. We, therefore, average the wave electric field power spectral densities over all MLT when the satellite is within $\pm 15^\circ$ of the VLF transmitter and subsequently take into account the other longitudes, where we assume that the power from the VLF transmitter is zero, by dividing the result by 12.

The EMFISIS HFR measures a single component of the wave electric field. We estimate the full wave electric field spectral density by multiplying the one component by a factor of 3 as in previous work (Agapitov et al., 2014; Ma et al., 2017). We then calculate the electric field intensity associated with any given VLF transmitter by multiplying the average wave power spectral density by the bandwidth of the frequency channel containing the bulk of the VLF transmitter power. We found that five VLF transmitters, NWC, GVT, NAA, NML, and unid25, had significant power in neighboring frequency bins. For these cases we summed the powers determined from each neighboring bin separately.

The electric field intensities, S_E , were then converted to magnetic field intensities, S_B , using the expression

$$S_B = \frac{1}{c^2} \left(1 - \frac{f_{pe}^2}{f(f - f_{ce})} \right) S_E \quad (1)$$

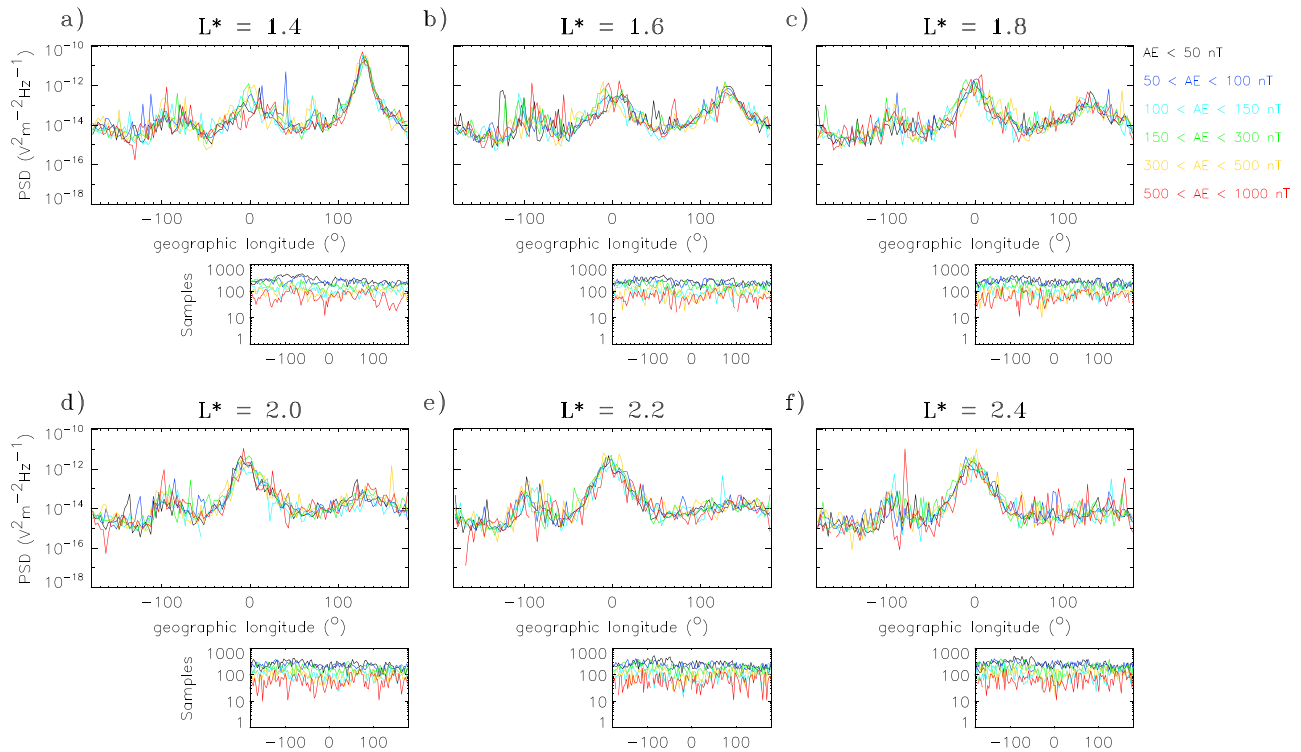


Figure 5. Plots of the average wave electric field power spectral density (PSDs) on the nightside in the frequency band 22.07–23.15 kHz mapped to the northern footprint of the satellite and displayed as a function of geographic longitude for different levels of geomagnetic activity (color coded). The plots are presented in order of increasing L^* , ranging from $L^* = 1.4$ (a) to $L^* = 2.4$ (f). The average power spectral densities are shown in the large panels and the corresponding sampling distributions in the small panels.

derived from Maxwell's third equation and assuming a cold plasma dispersion relation for parallel-propagating ($\psi = 0^\circ$) whistler mode waves. The E to B conversion requires models of f_{pe} and f_{ce} . We calculate the average value of f_{pe} as a function of L^* for $AE < 300$ nT using the f_{pe} measurements from the EMFISIS HFR within 10° of the geomagnetic equator. The results are plotted as the red solid trace in the top panel of Figure 6. The values generally increase with decreasing L^* , but this trend is reversed at the lowest L^* values due to the fact that the plasma frequency can exceed the upper frequency limit of the HFR

in this region. For comparison, the plasma frequency, derived from the statistical plasmaspheric density model of Ozhogin et al. (2012), valid for $1.3 \leq L < 4.5$, is plotted as the red dotted trace. The average values derived from the EMFISIS data depart from the model inside $L^* = 2.2$. For the wave electric field to wave magnetic field conversion we therefore use model values inside $L^* = 2.2$ and data values outside $L^* = 2.2$. We note that signals from VLF transmitters can occasionally be observed outside the plasmapause, but these events are rare (e.g., Carpenter & Miller, 1983) and tend to occur during active times (e.g., Foster et al., 2016) and thus will not significantly affect the derived average magnetic field wave intensities. We also calculate the average value of f_{ce} as a function of L^* for $AE < 300$ nT. The results are shown in the large panel in Figure 6 (black trace) for observations within 5° of the geomagnetic equator. Values for a dipole field are shown for comparison as the dotted trace, showing that, on average, during quiet and moderately active times ($AE < 300$ nT), departures from a dipole field are small in the inner belt and slot region. The corresponding sampling distributions are shown in the small panel.

There is still a question of whether one should use an MLT and longitude-averaged transmitter wave power when calculating diffusion coefficients or consider the diffusion as a function of MLT and longitude

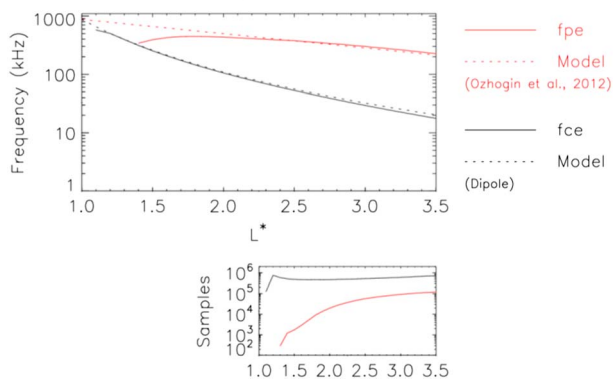


Figure 6. Plots of f_{pe} , red traces, and f_{ce} , black traces, as a function of L^* (top panel). The solid lines represent the values derived from the data, and the dashed lines represent model values. For f_{pe} the model values have been computed using the formula presented in Ozhogin et al. (2012) and for f_{ce} the model is a simple dipole. The corresponding sampling distributions, used to compute the values derived from the data, are shown in the bottom panel.

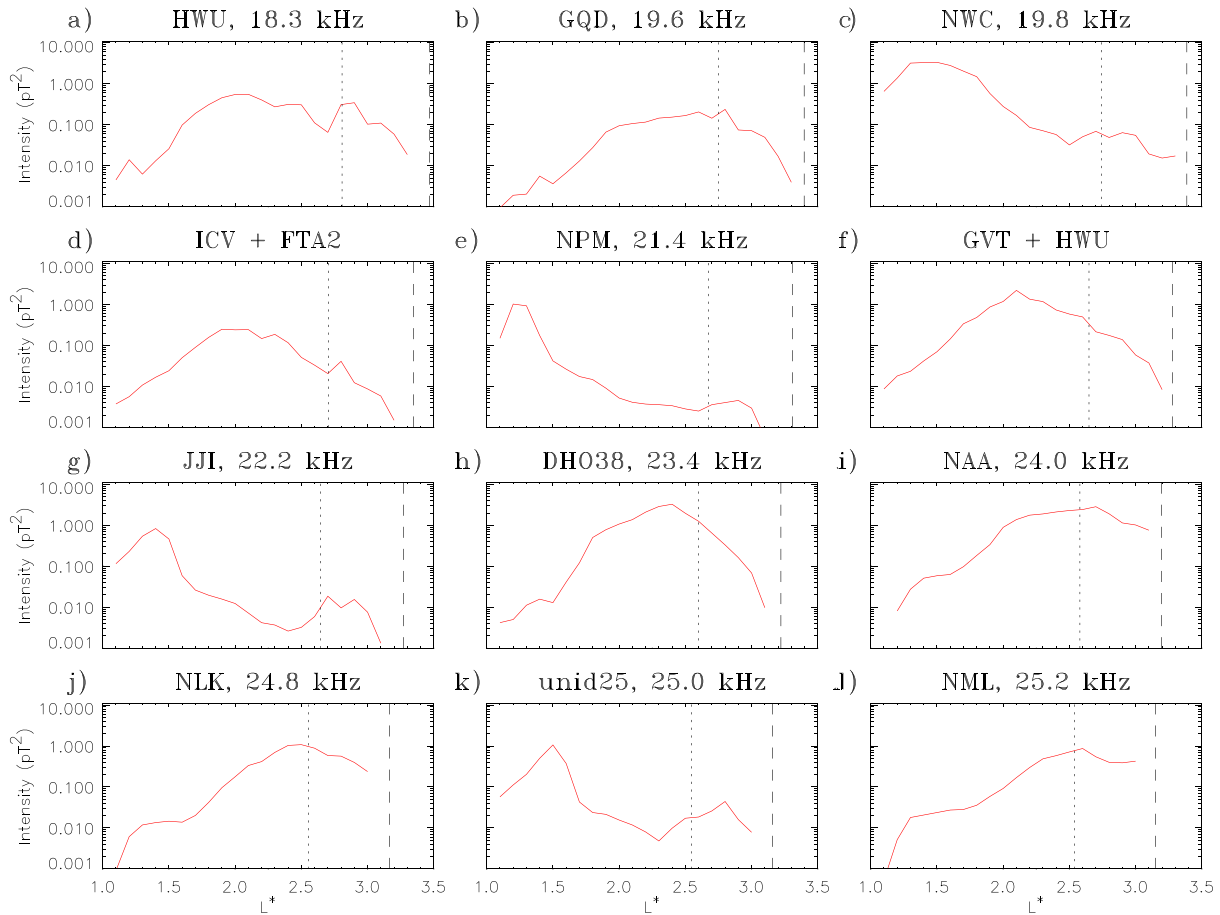


Figure 7. Plots of the average wave magnetic field intensity as a function L^* for each VLF transmitter, presented in order of increasing frequency (a to l). The vertical dashed and dotted lines denote the equatorial L^* values for which the transmitter frequency is equal to f_{ce} and $f_{ce}/2.0$, respectively.

of the transmitter. This is discussed in more detail in our companion paper (Ross et al., 2019). In this section we average over MLT and longitude to provide measurements that can be compared to previous work. The average wave magnetic field intensities as a function of L^* are shown for each VLF transmitter in Figure 7. The average peak powers cover approximately 2 orders of magnitude and range from 0.05 pT^2 for TBB (not shown) to $\sim 4 pT^2$ for NWC, DHO38, and NAA. Strong wave power at low L^* , $L^* < 1.7$, is seen in Figures 7c, 7e, 7g, and 7k. This strong wave power is associated with VLF transmitters located inside $L^* = 1.5$, namely, NWC, NPM, JJI, and unid25, respectively. The largest average power from this set of VLF transmitters is from NWC and is about a factor of 4 times larger than the average peak powers from NPM, JJI, and unid25, all of which peak around 1 pT^2 . Strong wave power at higher L^* , $L^* > 2.0$, is seen primarily in Figures 7f, 7h, 7i, 7j, and 7l. This strong wave power is associated with the strongest VLF transmitters located outside $L^* = 2.0$, namely, GVT + HWU, DHO38, NAA, NLK, and NML. The largest peak average power from this set of VLF transmitters comes from DHO38 and NAA and is about a factor of 4 times larger than the average peak powers from NLK and NML and twice the peak power of GVT+HWU.

The average wave power from all of the VLF transmitters is shown as a function of L^* in Figure 8 (red trace). Given the large range of variability between the average wave power observed from the individual VLF transmitters, it is interesting to see that the average wave power from all the VLF transmitters in the region $1.2 < L^* < 3.0$ varies by only a factor of 3, ranging from 3 to 9 pT^2 . On the same plot we show the average wave power as a function of L^* from the three strongest VLF transmitters, NWC (black trace), DHO38 (purple trace), and NAA (blue trace) and their combined sum (green trace). This plot shows that, in the inner belt and slot region, approximately 50% of the average wave power from all of the VLF transmitters combined effectively comes from these three VLF transmitters.

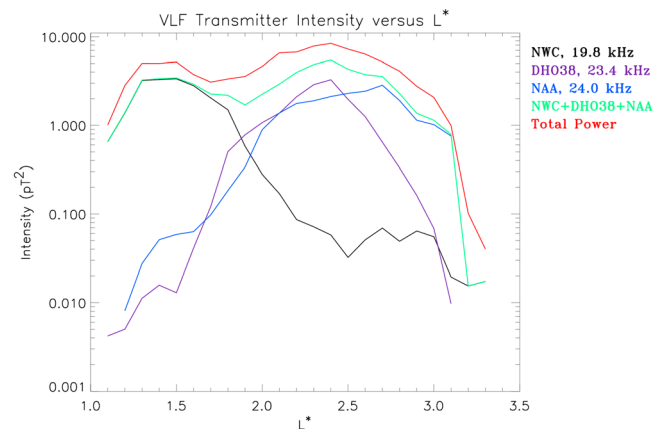


Figure 8. Plots of the average wave magnetic field intensity as a function L^* for the three strongest VLF transmitter signals (color coded), their sum (green trace), and the total intensity from all of the VLF transmitters combined (red trace).

6. Discussion

Power peaks primarily on the nightside for the VLF transmitters at low geographic latitudes. This is due to the fact that the D region transmission is least attenuated at night, when the ionosphere is in darkness (e.g., Cohen et al., 2012; Helliwell, 1965, Figure 3.35). At higher latitudes the peak power extends further in MLT, typically by up to 2 hr both pre-18:00 and post-06:00 MLT, due to more extensive periods of nighttime in the winter months, enabling more power to escape into the magnetosphere during these periods. Power near noon is typically orders of magnitude less than that observed on the nightside for all VLF transmitter signals, implying that pitch angle scattering from a given transmitter will be much more effective when the transmitter site is in darkness. This is consistent with DEMETER observations of the enhancements of electrons seen in the drift loss cone east of NWC, which are only observed when NWC is in darkness (Gamble et al., 2008).

The observed power from any given VLF transmitter is tightly confined in longitude and peaks on the nightside. Here the peak power typically falls by a factor of 10 within 10° longitude of the location of the peak signal. At any given time the observed power is thus strongest when the satellite is located on the nightside of the Earth and when one of the geographic footprints lies in the vicinity of an operational VLF transmitter. This raises the interesting question of how best to treat these signals when computing diffusion coefficients. Is it valid, for example, to average the equatorial wave power over all UT and MLT as a function of L^* , or should MLT and longitude be taken into account? This intriguing question is fully addressed in our companion paper (Ross et al., 2019).

To compare with previous measurements and for diffusion calculations, we convert the wave electric field to the wave magnetic field. We assume a cold plasma and parallel propagation. This is likely to be a good assumption for $L^* > 1.5$ since these waves are highly ducted in the plasmasphere (Clilverd et al., 2008). At lower values of L^* a significant proportion of the wave power is nonducted (Clilverd et al., 2008) with wave normal angles around $60\text{--}70^\circ$ near the geomagnetic equator (Kulkarni et al., 2008). In this case the estimated power is an upper limit. Using the full cold plasma dispersion relation, we find that the wave magnetic field derived from the wave electric field assuming a wave normal angle of 65° is a factor of ~ 0.65 less than that derived for parallel propagation for transmitters in the region $1.2 < L^* < 1.5$ (Ross et al., 2019). This would reduce the total intensity from 5 to 3 pT^2 in the region $1.3 \leq L^* \leq 1.4$. We conclude that the total average wave power from all VLF transmitters lies in the range 3–9 pT^2 in the region $1.3 < L^* < 3.0$. Approximately 50% of this power comes from three VLF transmitters, NWC, NAA, and DHO38.

The enhanced emissions on the dawnside during geomagnetically active conditions decrease in intensity with increasing frequency. For the frequency bins used in this study the average wave power is strongest in the lowest-frequency bin in Table 2, where the strongest enhancements are observed in the region $2.5 < L^* < 3.1$, corresponding to normalized frequencies in the range $0.33 < f_{ce} < 0.63$. At 10 kHz, the lowest

frequency of the HFR, the strongest dawnside emissions are again seen during active conditions but at this frequency, further out in the region $3.1 < L^* < 3.7$, corresponding to normalized frequencies in the range $0.34 < f_{ce} < 0.58$. The location, activity dependence, and normalized frequency range suggest that these emissions are a mixture of upper and lower band chorus (Li et al., 2011; Meredith et al., 2001, 2012).

We investigated the dependence on geomagnetic activity, using the *AE* index, for each VLF transmitter as a function of longitude and L^* . We found no significant dependence on *AE* for any of the VLF transmitters. This result is consistent with observations of the signals from low- and middle-latitude VLF transmitters ($L < 2.6$) made by the DEMETER satellite which showed no detectable variations in intensity with geomagnetic activity as monitored by the *Kp* index (Cohen & Inan, 2012). However, more recently, Ma et al. (2017) have suggested that the combined wave power of the VLF transmitters in the region $2 < L < 3$ increases with geomagnetic activity, most notably when $Kp > 4$. The increase in wave power observed by Ma et al. (2017) in the region $2 < L < 3$ for $Kp > 4$ is inconsistent with the results presented here and with the DEMETER observations (Cohen & Inan, 2012) and could be due to the presence of chorus signatures which add to the transmitter signals during the most active periods in this region.

VLF transmitters are essential for communications with submarines and operate most of the time. However, they are occasionally turned off for repairs and maintenance. Most transmitters have a weekly, daytime maintenance period, but since the observed wave power is typically orders of magnitude less on the dayside as compared to the nightside, the MLT and longitude-averaged wave power will not be significantly affected by these maintenance periods. Of the three major transmitters in this study, only NWC had a significant period of downtime from 1 September 2013 to 12 October 2013, resulting in the loss of 42-day coverage. This would have only a small effect on the MLT and longitude-averaged wave power for NWC over the 5-year period—of the order of a 2% underestimate in the average wave power for this VLF transmitter.

The signature from the VLF transmitter unid25 in Mopko, South Korea, is clear and unambiguous (Figures 3g and 4g). However, attempts to identify this signature using ground-based observations from the AARDVARK network of VLF receivers (Clilverd et al., 2009) have, so far, been unsuccessful. This is unexpected since such a strong signature should be identifiable in the ground-based measurements, and all the other VLF transmitter signals used in this study are detected by the AARDVARK network. We do not have an explanation for this and are currently examining the data sets with a view to understanding the cause of this anomaly.

7. Conclusions

We have analyzed ~5 years of wave data from the Van Allen Probe A satellite to construct a new global model of the wave power in space from VLF transmitters. Our principle conclusions are as follows:

1. The average power peaks primarily on the nightside of the Earth for VLF transmitters at low geographic latitudes.
2. At higher latitudes the peak average power extends further in MLT due to more extensive periods of nighttime in the winter months.
3. Nighttime power is typically orders of magnitude more than that observed near noon, implying that loss rates from a given VLF transmitter will also maximize in this region.
4. Geographically, the bulk of the power from each VLF transmitter is narrowly confined in longitude, typically falling to one tenth of the peak power within $\pm 10^\circ$ of the peak in the power.
5. The observed VLF transmitter power in the inner magnetosphere does not show any significant dependence on geomagnetic activity as monitored by the *AE* index.
6. In the region $1.3 < L^* < 3.0$ the combined average wave power from all of the VLF transmitters lies in the range 3–9 pT².
7. The bulk of the wave power observed in the inner magnetosphere comes from three VLF transmitters, NWC, DHO38, and NAA.

The new model of VLF transmitters presented in this paper has been used in our companion study to investigate the role of VLF transmitters in electron loss in the inner radiation belt and slot region. The results of this study are presented in Ross et al. (2019).

Acknowledgments

We acknowledge the NASA Van Allen Probes and Craig Kletzing for use of the EMFISIS data, available online (<https://emfisis.physics.uiowa.edu/data/index>). We also acknowledge the Radiation Belt Storm Probes ECT Science Operations and Data Center for the provision of the magnetic ephemeris data, available online (https://www.rbsp-ect.lanl.gov/data_pub/rbspa/MagEphem/). We thank the NSSDC Omniweb for the provision of the AE indices used in this paper. The research leading to these results has received funding from the Natural Environment Research Council (NERC) Highlight Topic Grant NE/P01738X/1 (Rad-Sat) and the NERC Grant NE/R016038/1. The results and data shown in this paper can be downloaded from the U.K. Polar Data Centre (<https://data.bas.ac.uk/>) and (<https://doi.org/10.5285/395408f5-0f0e-43b3-83c8-dfa719a1bb87>).

References

Abel, B., & Thorne, R. M. (1998a). Electron scattering loss in Earth's inner magnetosphere. 1. Dominant physical processes. *Journal of Geophysical Research*, *103*(A2), 2385–2396. <https://doi.org/10.1029/97JA02919>

Abel, B., & Thorne, R. M. (1998b). Electron scattering loss in Earth's inner magnetosphere. 2. Sensitivity to model parameters. *Journal of Geophysical Research*, *103*(A2), 2397–2407. <https://doi.org/10.1029/97JA02920>

Agapitov, O. V., Artemyev, A. V., Mourenas, D., Kasahara, Y., & Krasnoselskikh, V. (2014). Inner belt and slot region electron lifetimes and energization rates based on AKEBONO statistics of whistler waves. *Journal of Geophysical Research: Space Physics*, *119*, 2876–2893. <https://doi.org/10.1002/2014JA019886>

Albert, J. M. (1994). Quasi-linear pitch angle diffusion coefficients: Retaining high harmonics. *Journal of Geophysical Research*, *99*(A12), 23,741–23,745. <https://doi.org/10.1029/94JA02345>

Albert, J. M., Starks, M. J., Horne, R. B., Meredith, N. P., & Glauert, S. A. (2016). Quasi-linear simulations of inner radiation belt electron pitch angle and energy distributions. *Geophysical Research Letters*, *43*, 2381–2388. <https://doi.org/10.1002/2016GL067938>

Baker, D. N., Blake, J. B., Callis, L. B., Cummings, J. R., Hovestadt, D., Kanekal, S., et al. (1994). Relativistic electron acceleration and decay time scales in the inner and outer radiation belts: SAMPEX. *Geophysical Research Letters*, *21*, 409–412.

Baker, D. N., Kanekal, S. G., Horne, R. B., Meredith, N. P., & Glauert, S. A. (2007). Low-altitude measurements of 2–6 MeV electron trapping lifetimes at 1.5 = L = 2.5. *Geophysical Research Letters*, *34*, L20110. <https://doi.org/10.1029/2007GL031007>

Blake, J. B., Kolasinski, W. A., Fillius, R. W., & Mullen, E. G. (1992). Injection of electrons and protons with energies of tens of MeV into L < 3 on 24 March 1991. *Geophysical Research Letters*, *19*(8), 821–824.

Carpenter, D. L., & Miller, T. R. (1983). Rare ground-based observations of Siple VLF transmitter signals outside the plasmapause. *Journal of Geophysical Research*, *88*(A12), 10227–10232. <https://doi.org/10.1029/JA088iA12p10227>

Clilverd, M. A., Rodger, C. J., Gamble, R., Meredith, N. P., Parrot, M., Berthelier, J.-J., & Thomson, N. R. (2008). Ground-based transmitter signals observed from space: Ducted or nonducted? *Journal of Geophysical Research*, *113*, A04211. <https://doi.org/10.1029/2007JA012602>

Clilverd, M. A., Rodger, C. J., Thomson, N. R., Brundell, J. B., Ulich, T., Lichtenberger, J., et al. (2009). Remote sensing space weather events: Antarctic-arctic radiation-belt dynamic deposition-VLF atmospheric research Konsortium network. *Space Weather*, *7*, S04001. <https://doi.org/10.1029/2008SW000412>

Cohen, M. B., & Inan, U. S. (2012). Terrestrial VLF transmitter injection into the magnetosphere. *Journal of Geophysical Research*, *117*, A08310. <https://doi.org/10.1029/2012JA017992>

Cohen, M. B., Inan, U. S., & Paschal, E. (2009). Sensitive broadband ELF/VLF radio reception with the AWESOME instrument. *IEEE Transactions on Geoscience and Remote Sensing*, *48*, 3–17. <https://doi.org/10.1109/TGRS.2009.2028334>

Cohen, M. B., Lehtinen, N. G., & Inan, U. S. (2012). Models of ionospheric VLF absorption of powerful ground based transmitters. *Geophysical Research Letters*, *39*, L24101. <https://doi.org/10.1029/2012GL054437>

Datlowe, D. W., & Imhof, W. L. (1990). Cyclotron resonance precipitation of energetic electrons from the inner magnetosphere. *Journal of Geophysical Research*, *95*(A5), 6477–6491. <https://doi.org/10.1029/JA095iA05p06477>

Datlowe, D. W., Imhof, W. L., Fishman, G. J., & Finger, M. H. (1995). Local time and seasonal variations in the precipitation of energetic electrons from the inner radiation belt by cyclotron resonance with waves from powerful VLF transmitters. *Radio Science*, *30*(1), 47–55. <https://doi.org/10.1029/94RS02592>

Foster, J. C., Erickson, P. J., Baker, D. N., Jaynes, A. N., Mishin, E. V., Fennel, J. F., et al. (2016). Observations of the impenetrable barrier, the plasmapause, and the VLF bubble during the 17 March 2015 storm. *Journal of Geophysical Research: Space Physics*, *121*, 5537–5548. <https://doi.org/10.1002/2016JA022509>

Gamble, R. J., Rodger, C. J., Clilverd, M. A., Sauvaud, J.-A., Thomson, N. R., Stewart, S. L., et al. (2008). Radiation belt electron precipitation by man-made VLF transmissions. *Journal Geophysics Research*, *113*, A10211. <https://doi.org/10.1029/2008JA013369>

Helliwell, R. (1965). *Whistlers and related ionospheric phenomena*. Stanford California: Stanford University Press.

Horne, R. B., & Pitchford, D. (2015). Space weather concerns for all-electric propulsion satellites. *Space Weather*, *13*, 430–433. <https://doi.org/10.1002/2015SW001198>

Imhof, W. L., Reagan, J. B., Voss, H. D., Gaines, E. E., Datlowe, D. W., Mobilia, J., et al. (1983). Direct observation of radiation belt electrons precipitated by the controlled injection of VLF signals from a ground-based transmitter. *Geophysical Research Letters*, *10*, 361–364. <https://doi.org/10.1029/GL010i004p00361>

Inan, U. S., Chang, H. C., Helliwell, R. A., Imhof, W. L., Reagan, J. B., & Walt, M. (1985). Precipitation of radiation belt electrons by man-made waves: A comparison between theory and measurement. *Journal of Geophysical Research*, *90*(A1), 359–369. <https://doi.org/10.1029/JA090iA01p00359>

Kletzing, C. A., Kurth, W. S., Acuna, M., MacDowall, R. J., Torbert, R. B., Averkamp, T., et al. (2013). The electric and magnetic field instrument suite and integrated science EMFISIS on RBSP. *Space Science Reviews*, *179*, 127–181. <https://doi.org/10.1007/s11214-013-9993-6>

Kulkarni, P., Inan, U. S., Bell, T. F., & Bortnik, J. (2008). Precipitation signatures of ground-based VLF transmitters. *Journal of geophysical Research*, *113*, A07214. <https://doi.org/10.1029/2007JA012569>

Kurth, W. S., De Pascuale, S., Faden, J. B., Kletzing, C. A., Hospodarsky, G. B., Thaller, S., & Wygant, J. R. (2015). Electron densities inferred from plasma wave spectra obtained by the waves instrument on Van Allen Probes. *Journal of Geophysical Research: Space Physics*, *120*, 904–914. <https://doi.org/10.1002/2014JA020857>

Li, W., Bortnik, J., Thorne, R. M., & Angelopoulos, V. (2011). Global distribution of wave amplitudes and wave normal angles of chorus waves using THEMIS wave observations. *Journal of Geophysical Research*, *116*, A12205. <https://doi.org/10.1029/2011JA017035>

Li, W., Ma, Q., Thorne, R. M., Bortnik, J., Kletzing, C. A., Kurth, W. S., et al. (2015). Statistical properties of plasmaspheric hiss derived from Van Allen Probes data and their effects on radiation belt electron dynamics. *Journal of Geophysical Research: Space Physics*, *120*, 3393–3405. <https://doi.org/10.1002/2015JA021048>

Lyons, L. R., & Thorne, R. M. (1973). Equilibrium structure of radiation belt electrons. *Journal of Geophysical Research*, *78*(13), 2142–2149. <https://doi.org/10.1029/JA078i013p02142>

Lyons, L. R., Thorne, R. M., & Kennel, C. F. (1972). Pitch angle diffusion of radiation belt electrons within the plasmasphere. *Journal of Geophysical Research*, *77*(19), 3455–3474. <https://doi.org/10.1029/JA077i019p03455>

Ma, Q., Mourenas, D., Li, W., Artemyev, A., & Thorne, R. M. (2017). VLF Waves from ground-based transmitters observed by the Van Allen Probes: Statistical model and effects on plasmaspheric electrons. *Geophysical Research Letters*, *44*, 6483–6491. <https://doi.org/10.1002/2017GL073885>

Malaspina, D. M., Jaynes, A. N., Boulé, C., Bortnik, J., Thaller, S. A., Ergun, R. E., et al. (2016). The distribution of plasmaspheric hiss wave power with respect to plasmapause location. *Geophysical Research Letters*, *43*, 7878–7886. <https://doi.org/10.1002/2016GL069982>

- Mauk, B. H., Fox, N. J., Kanekal, S. G., Kessel, R. L., Sibeck, D. G., & Ukhorskiy, A. (2012). Science objectives and rationale for the Radiation Belt Storm Probes mission. In N. Fox (Ed.), *The Van Allen Probes Mission*. Boston, MA: Springer.
- Meredith, N. P., Horne, R. B., & Anderson, R. R. (2001). Substorm dependence of chorus amplitudes: Implications for the acceleration of electrons to relativistic energies. *Journal of Geophysical Research*, *106*(A7), 13165–13178. <https://doi.org/10.1029/2000JA900156>
- Meredith, N. P., Horne, R. B., Clilverd, M. A., Horsfall, D., Thorne, R. M., & Anderson, R. R. (2006). Origins of plasmaspheric hiss. *Journal of Geophysical Research*, *111*, A09217. <https://doi.org/10.1029/2006JA011707>
- Meredith, N. P., Horne, R. B., Glauert, S. A., & Anderson, R. R. (2007). Slot region electron loss timescales due to plasmaspheric hiss and lightning generated whistlers. *Journal of Geophysical Research*, *112*, A08214. <https://doi.org/10.1029/2006JA012413>
- Meredith, N. P., Horne, R. B., Glauert, S. A., Baker, D. N., Kanekal, S. G., & Albert, J. M. (2009). Relativistic electron loss timescales in the slot region. *Journal of Geophysical Research*, *114*, A03222. <https://doi.org/10.1029/2008JA013889>
- Meredith, N. P., Horne, R. B., Kersten, T., Li, W., Bortnik, J., Sicard, A., & Yearby, K. (2018). Global model of plasmaspheric hiss from multiple satellite observations. *Journal of Geophysical Research: Space Physics*, *124*, 1660–1678. <https://doi.org/10.1002/2018JA025226>
- Meredith, N. P., Horne, R. B., Sicard-Piet, A., Boscher, D., Yearby, K. H., Li, W., & Thorne, R. M. (2012). Global model of lower band and upper band chorus from multiple satellite observations. *Journal of Geophysical Research*, *117*, A10225. <https://doi.org/10.1029/2012JA017978>
- Meredith, N. P., Horne, R. B., Thorne, R. M., Summers, D., & Anderson, R. R. (2004). Substorm dependence of plasmaspheric hiss. *Journal of Geophysical Research*, *109*, A06209. <https://doi.org/10.1029/2004JA010387>
- Olson, W. P., & Pfitzer, K. (1977). Magnetospheric magnetic field modeling (*Annual Scientific Report*). Arlington, Va: AFOSR Contract F44620-75-c-0033, Air Force Off. of Sci Res.
- Ozhogin, P., Tu, J., Song, P., & Reinisch, B. W. (2012). Field-aligned distribution of the plasmaspheric electron density: An empirical model derived from the IMAGE RPI measurements. *Journal of Geophysical Research*, *117*, A06225. <https://doi.org/10.1029/2011JA017330>
- Roederer (1970). *Dynamics of geomagnetically trapped radiation*, pp. 166. New York: Springer-Verlag.
- Ross, J. P. J., Meredith, N. P., Glauert, S. A., Horne, R. B., & Clilverd, M. A. (2019). Effects of VLF transmitter waves on the inner belt and slot region. *Journal of Geophysical Research: Space Physics*, *124*. <https://doi.org/10.1029/2019JA026716>
- Selesnick, R. S., Albert, J. M., & Starks, M. J. (2013). Influence of a ground-based VLF radio transmitter on the inner electron radiation belt. *Journal of Geophysical Research: Space Physics*, *118*, 628–635. <https://doi.org/10.1002/jgra.50095>
- Selesnick, R. S., Su, Y.-J., & Blake, J. B. (2016). Control of the innermost electron radiation belt by large-scale electric fields. *Journal of Geophysical Research: Space Physics*, *121*, 8417–8427. <https://doi.org/10.1002/2016JA022973>
- Smith, E. J., Frandsen, A. M. A., Tsurutani, B. T., Thorne, R. M., & Chan, K. W. (1974). Plasmaspheric hiss intensity variations during magnetic storms. *Journal of Geophysical Research*, *79*(16), 2507–2510. <https://doi.org/10.1029/JA079i016p02507>
- Spasojevic, M., Shprits, Y. Y., & Orlova, K. (2015). Global empirical models of plasmaspheric hiss using Van Allen Probes. *Journal of Geophysical Research: Space Physics*, *120*, 10,370–10,383. <https://doi.org/10.1002/2015JA021803>
- Su, Y.-J., Selesnick, R. S., & Blake, J. B. (2016). Formation of the inner electron radiation belt by enhanced large-scale electric fields. *Journal of Geophysical Research: Space Physics*, *121*, 8508–8522. <https://doi.org/10.1002/2016JA022881>
- Thorne, R. M., Church, S. R., Malloy, W. J., & Tsurutani, B. T. (1977). The local time variation of ELF emissions during periods of substorm activity. *Journal of Geophysical Research*, *82*(10), 1585–1590. <https://doi.org/10.1029/JA082i010p01585>
- Thorne, R. M., Smith, E. J., Fiske, K. J., & Church, S. R. (1974). Intensity variation of ELF hiss and chorus driving isolated substorms. *Geophysical Research Letters*, *1*(5), 193–196. <https://doi.org/10.1029/GL001i005p00193>
- Tsurutani, B. T., Falkowski, B. J., Pickett, J. S., Santolik, O., & Lakhina, G. S. (2015). Plasmaspheric hiss properties: Observations from Polar. *Journal of Geophysical Research: Space Physics*, *120*, 414–431. <https://doi.org/10.1002/2014JA020518>
- Vampola, A. L., & Kuck, G. A. (1978). Induced precipitation of inner zone electrons. 1. Observations. *Journal of Geophysical Research*, *83*(A6), 2543–2551. <https://doi.org/10.1029/JA083iA06p02543>
- Walt, M. (1964). The effects of atmospheric collisions on geomagnetically trapped electrons. *Journal of Geophysical Research*, *69*, 3947–3958.